PHYSICAL REVIEW B **103**, 174107 (2021)

Structural phase transition and its consequences for the optical behavior of $LaV_{1-x}Nb_xO_4$

Hemanshu Dua,[*] Rishabh Shukla,[*] and R. S. Dhaka[†]
Department of Physics, Indian Institute of Technology Delhi, Hauz Khas, New Delhi-110016, India

(Received 2 February 2021; revised 2 May 2021; accepted 3 May 2021; published 12 May 2021)

We present the structural, electronic, vibrational, and photoluminescence properties of polycrystalline $LaV_{1-x}Nb_xO_4$ ($x = 0$–0.2) samples at room temperature. The substitution of Nb at the V site shows the fascinating structural and optical behavior due to their isoelectronic character and larger ionic radii of Nb^{5+} as compared to the V^{5+}. The Rietveld refinement of x-ray diffraction patterns demonstrate that the $x = 0$ sample exists in a monoclinic ($P2_1/n$) phase, whereas for the $x > 0$, both monoclinic and scheelite-tetragonal ($I4_1/a$) phases coexist in a certain proportion. Interestingly, a monotonous enhancement in the Raman spectral intensity with Nb substitution is correlated with the substitution induced increase in the scheelite-tetragonal phase. The x-ray absorption measurements reveal that the La ions exist in a trivalent oxidation state, while V and Nb cations possess 5+ oxidation state in tetrahedral coordination. Moreover, the Fourier-transform infrared (FTIR) spectra indicate that the Nb substitution give origin to some additional IR modes owing to the deformation of the VO_4^{3-} tetrahedra and mixing of monoclinic and tetragonal phases. The photoluminescence measurements on these samples exhibit broadband spectra and their deconvolution designate the availability of more than one electron-hole pairs recombination center.

DOI: 10.1103/PhysRevB.103.174107

I. INTRODUCTION

Orthovanadates are an eminent class of compounds with technological and fundamental significance, which have been extensively utilized as luminescent materials, polarizers, catalysts, biological sensors, battery electrodes, alternatives in green technologies, etc. [1–5]. These compounds exhibit phenomenon of temperature and pressure-dependent structural phase transformation [6,7], which was debated for a long time among the researchers for its order type [8]. In recent years, rare earth orthovanadates having a general formula of RVO_4 (R = rare-earth ion) have gained tremendous popularity for their useful applications in the area of solar cells [9,10], thin film phosphors [11], photocatalysis [12,13], etc. For enhancement in the optical performance of the orthovanadate compounds, researchers predominantly follow three paths, which can be defined as the substitution of metal cations [14], coupling with the other metal oxides [15], and synthesis of these compounds with various novel routes [16–18]. Primarily, the RVO_4 materials are known to crystallize into two polymorphs, namely monoclinic (m) monazite type (space group: $P2_1/n$, $Z = 4$) and tetragonal (t) zircon type (space group: $I4_1/amd$, $Z = 4$). Note that the space group $P2_1/n$ is defined as a nonconventional setting of the standard $P2_1/c$ space group (No. 14) and can be obtained by changing the basis vector in the matrix transformation of $P2_1/c$ [19]. In a monazite structure, R^{3+} cations form an edge-sharing nonahedra (RO_9) with distorted VO_4 tetrahedra along the c axis having four dissimilar V-O bonds [19], while tetragonal structure possesses edge-sharing dodecahedra (RO_8) and undistorted VO_4 tetrahedral chains parallel to the c axis with four identical V-O bonds [20]. It has been observed that the larger size of lanthanide ions (Ln^{3+}) favor monoclinic structure over a tetragonal one due to a higher oxygen coordination number [13,20]. Hence, the La^{3+} cations having the largest ionic radii in the Ln^{3+} series generally crystallize into the thermodynamically stable monoclinic structure and a metastable tetragonal structure [17,21], while other lanthanide orthovanadates predominantly crystallize into the zircon-type tetragonal structure [22].

Interestingly, the $LaVO_4$ can also be crystallized into a stable tetragonal structure in the form of nanocrystals/nanowires via the solution method but stabilizing the tetragonal structure is always been a challenging task [16,22,23]. A combination of the experiments like temperature-dependent photoconductivity, emission measurements, and different empirical models were employed to explain the complete energy level diagram of lanthanide-doped $LaVO_4$ compounds [24], which can be utilized to explain their luminescence properties and would help in the preparation of new luminescent materials. This is well known that the luminescence properties of lanthanide (Ln) doped rare-earth orthovanadates depend on the location of the $4f$ energy levels of the Ln dopants with respect to the valence and conduction band of the parent compound [25]. The t-$LaVO_4$ exhibits prominent photoluminescence properties as compared to its m counterpart because the t-$LaVO_4$ has four sigma bonds of angle 153°, which leads to the efficient transfer of energy, whereas in m-$LaVO_4$ the bond angles are smaller than t-$LaVO_4$, which results in the less effective transfer of energy [26]. The first-principles calculations for $LaVO_4$ polymorph performed using plane-wave pseudopotential method suggest that the m-$LaVO_4$ has an indirect band

---

[*] H.D. and R.S. contributed equally to this work.

[†] rsdhaka@physics.iitd.ac.in

gap of 3.5 eV, while the t-$LaVO_4$ has a direct band gap of 3 eV [27]. Thus, the phase transformation from m to t structure leads to a significant increase in the photoluminescent properties of $LaVO_4$, which are attributed to the structural difference of m and t phases.

In recent years, intensive research is being carried out in order to ameliorate the optical properties of $LaVO_4$ via substituting M^+ (Li), M^{2+} (Mg, Sr, etc.), M^{3+} (Eu, Sm, etc.), and M^{4+} (Sn, Zr, etc.) ions at La site [11,28–34], however, enhancement in the performance with the substitution at V site still has room to explore for the researchers, where only a report of Mn^{4+} cationic substitution induced catalytic properties are present in the literature [35]. Therefore, in order to enhance the optical performance of the $LaVO_4$ compound with B-site substitution, we have chosen the isoelectronic Nb^{5+} cations having a larger ionic radius of 0.48 Å as compared to V^{5+} (0.355 Å) ions [21]. Moreover, the end member $LaNbO_4$ is well known for its multifunctional applications in phosphors and scintillators [36,37], great tunability [38], and an efficient blue luminescence material when excited with a UV/x-ray source [39]. Also, the $LaNbO_4$ manifests a second-order temperature-dependent structural phase transformation in a temperature range of $500 \pm 20\,^{\circ}\mathrm{C}$ from a fergusonite-monoclinic (f-m) phase (space group: $I2/a$, No. 15) into a scheelite-tetragonal (s-t) phase (space group: $I4_1/a$, No. 88) [40,41]. Both phases (f-m and s-t) of $LaNbO_4$ compound consist of the NbO_4 tetrahedra and LaO_8 dodecahedra, which reflects the 12 triangular lattices [41]. The s-t structure has all 4×Nb-O equal bond lengths including two sets of 4×La-O bonds, whereas in the f-m phase two sets of Nb-O bonds appear with four pairs of La-O bond lengths [41]. This scheelite-tetragonal (s-t) phase is known as a close-packed (denser) polymorph with a volume reduction of nearly 10% with respect to the standard zircon-type tetragonal phase [6]. Moreover, a fergusonite to scheelite transformation is obtained from the cyclic rotation of axes with a transformation matrix and the long axis (unique b axis) in the fergusonite phase becomes the c axis of the scheelite phase with a gradual change of β from 94° to 90° [41,42]. These tetragonal phases in the orthovanadates were known to possess remarkable optical properties and hence be explored for their practical applications [43].

Therefore, in this paper we investigate the structural, electronic, vibrational, and photoluminescence properties of $LaV_{1-x}Nb_xO_4$ ($x = 0$–0.2). The Rietveld refinement of x-ray diffraction patterns demonstrates the monoclinic ($P2_1/n$) phase ($x = 0$), and appearance of an additional scheelite-tetragonal ($I4_1/a$) phase for the $x > 0$ samples. The room temperature x-ray absorption spectroscopy (XAS) measurements affirm the presence of trivalent La cations and a pentavalent oxidation state of V and Nb ions in tetrahedral coordination. The larger ionic radii of Nb^{5+} as compared to V^{5+} results in the structural phase transformation from a monoclinic to a scheelite-tetragonal. Moreover, an enhancement in the Raman spectral intensity is related to the increase in the tetragonal phase with the Nb substitution at V site. Furthermore, additional infrared modes in the Fourier-transform infrared (FTIR) spectra were observed due to the Nb induced structural transformation. In the room temperature PL measurements, we found that the strongly overlapped spectra can be deconvoluted into six peaks, where each emission process involves separate energy levels.

II. EXPERIMENT

The $LaV_{1-x}Nb_xO_4$ ($x = 0$–0.2) samples were prepared via solid-state reaction method by mixing V_2O_5 (99.6%, Sigma), Nb_2O_5 (99.99%, Sigma), and La_2O_3 (99.99%, Sigma) in the stoichiometric amount as initials, where La_2O_3 was predried at 900 °C for 6 h to remove moisture. The mixture was homogeneously ground for 8 h, followed by calcination at 1000 °C for 17 h, then the obtained mixture was reground and sintered at 1200 °C for 13 h. To improve the crystallinity of prepared samples, final sintering was done at 1250 °C for 13 h. We have also sintered the Nb substituted samples ($x = 0.1$ and 0.2) at 1450 °C for 13 h to explore the sintering temperature-induced phase transformation. The powder x-ray diffraction (XRD) data of prepared polycrystalline $LaNb_xV_{1-x}O_4$ ($x = 0$–0.2) samples were recorded using CuK_α radiation ($\lambda = 1.5406$ Å) from Rigaku Ultima IV, Ri x-ray diffractometer. The Rietveld refinement of recorded XRD patterns were accomplished using FullProf software [44] with background fitted using linear interpolation between the data points. The x-ray absorption measurements were recorded at room temperature in the transmission mode at La-L_2, Nb-K, and La-L_3 + V-K edges using the scanning EXAFS beamline (BL-09), Indus-2, RRCAT, Indore, India. The energy-dispersive x-ray analysis (EDX) was performed with the Zeiss EVO 18 at an operating voltage of 20 keV inside a vacuum chamber. The Raman spectra were recorded with the Renishaw inVia confocal Raman microscope using a 532 nm laser with grating 2400 lines/mm, 20× objective, and a power of 0.05 mW. The FTIR spectra were recorded using the Thermo Scientific Nicolet iS50 FT-IR spectrophotometer in the attenuated total reflection (ATR) mode within the range of 400–4000 cm^{-1}. This instrument has a separate assembly for the measurement of FTIR spectra in the ATR mode. In the ATR mode, a diamond crystal was used as an ATR crystal and the sample was in fine powder form to ensure an intimate contact with the diamond crystal. First, we record the background spectrum for the ATR crystal and then measure the spectrum for each sample. In the paper the presented FTIR spectra for each sample are corrected with this background spectrum of the diamond. The photoluminescence (PL) spectra were recorded using the Horiba Jobin Yvon; LabRAM HR evolution system equipped with a UV laser of the wavelength of 325 nm (He-Cd laser, 30 mW). The PL spectra were recorded with the 325 nm excitation laser source, a 40× objective, 2400 lines/mm grating, and 3 mW laser power. A charged coupled device (CCD) detector was used for the data collection. Finally, the diffuse reflectance spectroscopic measurements were conducted using a Shimadzu UV-2450 spectrophotometer at a slit width of 5 mm.

III. RESULTS AND DISCUSSION

Figure 1 shows the Rietveld refined room temperature powder x-ray diffraction (XRD) patterns of polycrystalline $LaV_{1-x}Nb_xO_4$ ($x = 0$–0.2) samples. We observe that the measured XRD pattern is well fitted using a monoclinic space

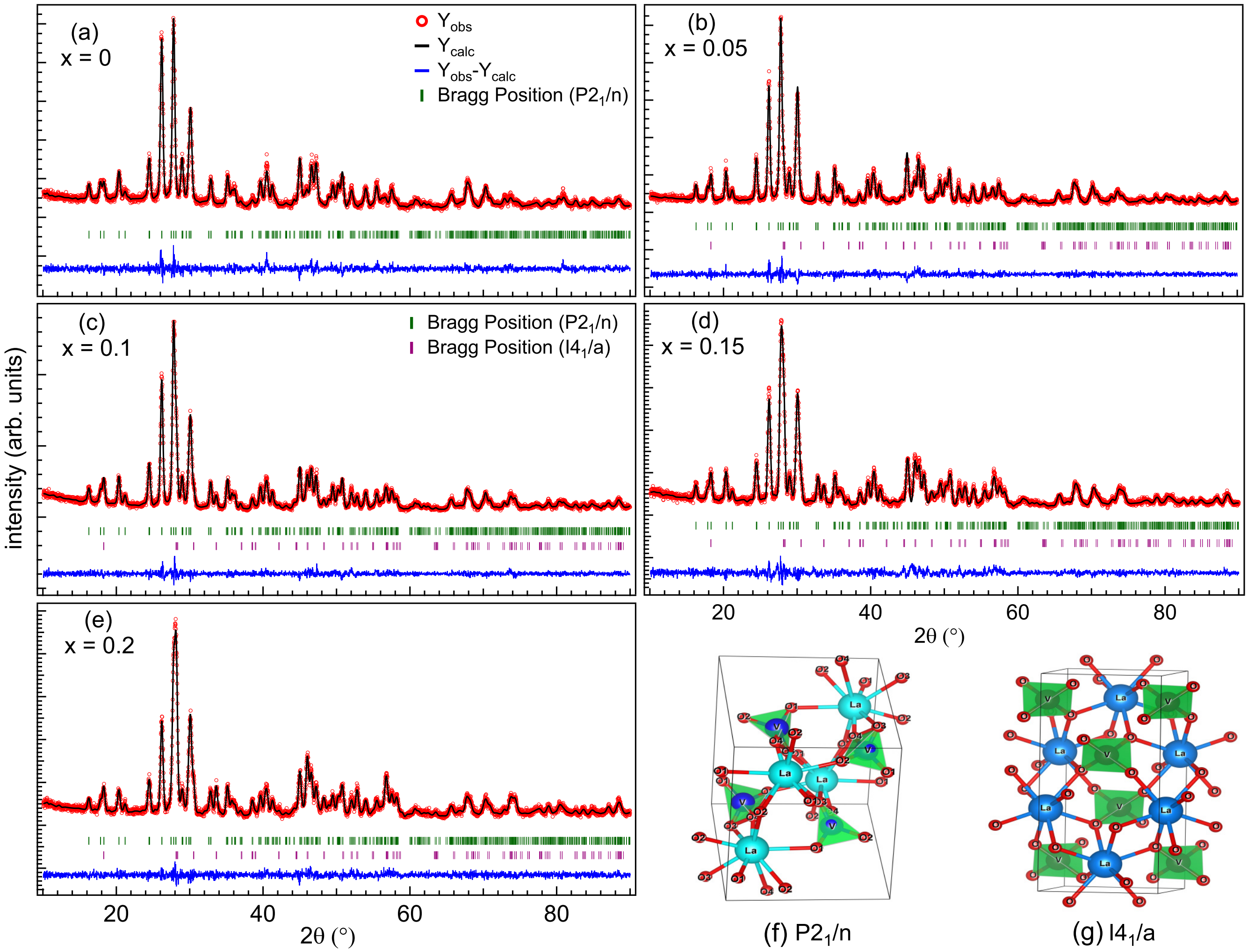

FIG. 1. The Rietveld refined x-ray diffraction patterns of $LaV_{1-x}Nb_xO_4$ (a) $x = 0$, (b) $x = 0.05$, (c) $x = 0.1$, (d) $x = 0.15$, and (e) $x = 0.2$ samples. Open red circles, black solid line, and blue solid line exhibit the experimental, simulated, and the difference between experimental and simulated spectra, respectively; green and magenta vertical markers present the Bragg positions corresponding to the $P2_1/n$ and $I4_1/a$ space groups, respectively. (f) and (g) Schematic unit cell diagrams for the monoclinic monazite ($P2_1/n$) and scheelite-tetragonal ($I4_1/a$) phases of $LaVO_4$ compound prepared using VESTA software [54], respectively, these phases are utilized to perform the Rietveld refinement of recorded x-ray diffraction patterns.

group ($P2_1/n$) for the $x = 0$ sample. Interestingly, the peak at 2θ value of 17.83° (110) diminishes in intensity, whereas the peak at 27.77° (120) splits into two peaks with the Nb substitution. We compare the XRD patterns of all the samples in Fig. S1(a) of Ref. [45]. Moreover, we observe that a few peaks emerge at 2θ values of 28.08°, 33.63°, 46.08°, 52.85°, 56.81°, and 58.25° with the Nb substitution, which corresponds to the scheelite-tetragonal phase with the (112), (020), (024), (116), (312), and (224) planes, respectively [46]. These changes in the XRD patterns are compared in Fig. S1(a) of Ref. [45], where the evolution of new peaks is highlighted with a black solid line. Notably, the XRD patterns for the $x > 0$ samples cannot be fitted by considering a single space group $P2_1/n$, as discussed and shown in Fig. S1(b) of Ref. [45]. Therefore, a combination of monoclinic ($P2_1/n$) and scheelite-tetragonal space groups ($I4_1/a$, No. 88) has been used to fit the XRD patterns for the $x = 0.05$–0.2 samples. We found that the Nb substitution induced structural transformation prevail in the samples for $x \geqslant 0.05$ concentration due to the larger ionic radius of Nb^{5+} (0.48 Å) ions as compared to V^{5+} ions (0.355 Å) in a tetrahedral coordination [21]. Note that the phenomenon of structural phase transformation from monoclinic ($P2_1/n$) to tetragonal ($I4_1/amd$) phase is well investigated in $LaVO_4$ with the cationic substitution of other lanthanides (Ln^{3+}) via reducing the average ionic radii of the atoms present at the La site, as the structural transformation into tetragonal phase lead to the remarkable enhancement in the photoluminescence properties [26,29]. Interestingly, in our case the substitution of Nb cations at V site lead to the structural phase transformation from monoclinic ($P2_1/n$) to a scheelite-tetragonal ($I4_1/a$) phase. Since the end members $LaVO_4$ and $LaNbO_4$ exist in the monoclinic monazite ($P2_1/n$) and fergusonite monoclinic ($I2/a$) phase in the ambient conditions, respectively, it was expected that the cationic substitution of Nb in $LaVO_4$ will induce a structural transformation from $P2_1/n$ to $I2/a$ space group [19,41,47]. However, there are several reports on the orthovanadate compounds, which explain a pressure-induced phase transformation

TABLE I. The Rietveld refined lattice parameters of polycrystalline $LaV_{1-x}Nb_xO_4$ ($x = 0$–0.2) samples with temperature-induced metastable scheelite-tetragonal phase for the $x = 0.1$ and 0.2 samples.

x	χ^2	Space group	a (Å)	b (Å)	c (Å)	β (deg)	Volume (Å^3)	Sintering temperature
0	1.09	$P2_1/n$	7.0413(6)	7.2759(6)	6.7172(6)	104.850(6)	332.64(5)	1250°C
0.05	1.05	$P2_1/n$ - 94%	7.0416(3)	7.2777(4)	6.7235(4)	104.911(5)	332.96(3)	1250°C
		$I4_1/a$ - 6%	5.3312(12)	5.3312(12)	11.712(5)	90	332.88(18)	
0.1	1.03	$P2_1/n$ - 88%	7.0409(3)	7.2769(4)	6.7230(4)	104.896(5)	332.88(3)	1250°C
		$I4_1/a$ - 12%	5.3323(5)	5.3323(5)	11.7115(16)	90	333.00(6)	
0.15	1.1	$P2_1/n$ - 84%	7.0431(4)	7.2781(4)	6.7261(5)	104.932(6)	333.14(3)	1250°C
		$I4_1/a$ - 16%	5.3313(4)	5.3313(4)	11.7165(14)	90	333.01(5)	
0.2	1.14	$P2_1/n$ - 72%	7.0395(4)	7.2760(5)	6.7262(5)	104.921(6)	332.89(4)	1250°C
		$I4_1/a$ - 28%	5.3312(3)	5.3312(3)	11.7128(11)	90	332.89(4)	
0.1	1.44	$I4_1/a$	5.3248(2)	5.3248(2)	11.7311(6)	90	332.61(2)	1450°C
0.2	1.47	$I4_1/a$	5.3289(2)	5.3289(2)	11.7478(7)	90	333.60(3)	1450°C

between the various crystal symmetries, e.g., zircon-tetragonal, scheelite-tetragonal, fergusonite-monoclinic, and $BaWO_4$-II type, etc. [6,7,48–50]. This structural transformation from one phase to another is correlated to the occupation of f electrons of the lanthanide cations and their ionic radii [7].

Note that a competition between the scheelite to fergusonite and scheelite to $P2_1/n$ phase transition exists in the larger R cation compounds [51]. However, for a complete structural transformation, i.e., in order to synthesize the pure scheelite-tetragonal phase of RVO_4 compounds, a high hydrostatic pressure of about 25 GPa is required [6,52]. Here we found a phase transformation from the fergusonite to scheelite phase during the sample synthesis and at room temperature we obtained a signature of the scheelite phase in the recorded x-ray diffraction patterns of the final product [see Figs. 1(b)–1(e)]. Note that a fergusonite to scheelite transformation is second order and obtained from the cyclic rotation of axes using a transformation matrix and the long axis (unique b axis) in fergusonite phase transforms into the c axis of the scheelite phase. This phase transformation of the unit cell is well accompanied by the movement of the atoms (change in the Wyckoff positions), i.e., the La and V(Nb) cations move with the same magnitude, while the O atoms move in such a way that reduces the bond-length distortion index [49,53]. In short, the fergusonite phase is a compressed and less distorted version of the scheelite phase, with the β value of 94° as compared to 90° for scheelite phase. There is a very effective way to visualize these structural phase transformations using group-subgroup relations by making a Bärnighausen tree and applying the translationgleiche and klassengleiche transformations [53]. Since it is well known that the t-$LaVO_4$ possess the superior optical properties as compared to the phases with monoclinic symmetry [43], hence Nb substitution induced emergence of scheelite-tetragonal phase lead to an enhancement of luminescence properties in the $LaV_{1-x}Nb_xO_4$ samples. The Rietveld refined unit cell parameters are presented in Table I, where the lattice parameter values for the $x = 0$ sample are in good agreement with the previous reports [19,47]. Moreover, the lattice parameter values for the $x = 0.05$ sample increases with the Nb substitution and a scheelite phase also emerges. For the samples $x > 0.05$ we do not observe a systematic change in the unit cell parameters, which possibly caused by the enhancement in the proportion of the scheelite phase. Guo *et al.* have synthesized the $x = 0.1$ sample to study its microwave dielectric properties and obtained a composite phase of scheelite and monoclinic; however, they did not extract the relative phase fraction and lattice parameters [47].

It has been reported that the metastable structure of tetragonal $LaVO_4$ is commonly stabilized through a "soft chemical" process, e.g., the hydrothermal method was used to stabilize the tetragonal phase of $LaVO_4$ [17,34]. Moreover, there are few studies related to the hydrostatic pressure-dependent structural phase transformation from m- to t-$LaVO_4$ phase [49,50]. Interestingly, in order to obtain a stable tetragonal phase, which shows superior luminescent properties, we use high-temperature sintering of $LaV_{1-x}Nb_xO_4$ ($x = 0.1$, 0.2) samples at 1450 °C for 13 h and found a reversible transformation into a metastable scheelite-tetragonal phase [see Figs. 2(a) and 2(b)]. However, this metastable phase is again transformed to the initial stable phase (a mixture of monoclinic and scheelite-tetragonal phases). The presence of a scheelite-tetragonal phase in the $x = 0.1$ and 0.2 samples at room temperature in a certain fraction act as a nucleation center to transform this into a complete scheelite-tetragonal phase. The Rietveld refinement of this metastable phase in $LaV_{1-x}Nb_xO_4$ ($x = 0.1$, 0.2) samples is performed using the space group $I4_1/a$ (No. 88) and shown in Figs. 2(a) and 2(b). The Rietveld refined lattice parameters for the metastable phase are also included in Table I. We observe a monotonous increase in the lattice parameters and unit cell volume with an increase in the Nb concentration. Interestingly, this scheelite-tetragonal phase induced by the substitution of larger size Nb ions is further supported by the sintering temperature, where we observe a complete reversible structural phase transformation. Therefore, this phase transformation induced with the high-temperature sintering in the $x = 0.1$ and 0.2 samples manifests that a scheelite-tetragonal phase can be stabilized at higher temperatures. The energy dispersive x-ray measurements performed at room temperature (not shown here) confirm the stoichiometric compositional ratio of constituent

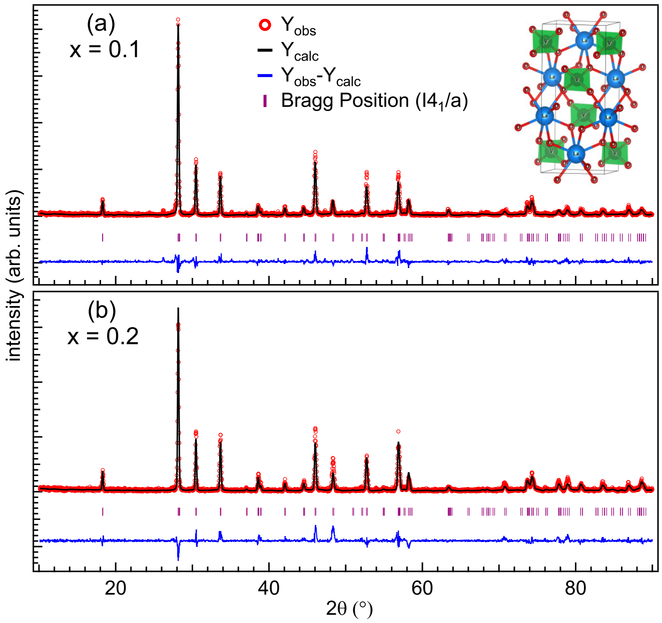

FIG. 2. The Rietveld refined x-ray diffraction patterns of metastable $LaV_{1-x}Nb_xO_4$ (a) $x = 0.1$ and (b) $x = 0.2$ samples sintered at 1450 °C, fitted using a scheelite-tetragonal phase (space group, $I4_1/a$, No. 88). Open red circles, black solid line, and blue solid line exhibit the experimental, simulated, and the difference between experimental and simulated spectra, respectively. Magenta vertical markers present the Bragg positions corresponding to the $I4_1/a$ space group, inset in (a) shows the schematic unit cell diagram for the scheelite-tetragonal phase utilized to fit the recorded x-ray patterns.

TABLE II. The experimentally observed frequencies (ω_{obs}) of the individual Raman modes in polycrystalline monazite $LaVO_4$ sample at room temperature with a position accuracy within ±1 cm^{-1}. The peak positions of these modes are compared with the reported theoretical (ω_{th}) values in Refs. [27,49] and previously obtained experimental values (ω_{expt}) in Refs. [49,50,57]. The values (ω_{obs}) are in close agreement with Ref. [49]; therefore the same has been adopted for the mode assignment in the present paper.

Peak	ω_{obs} (cm^{-1})	ω_{th} [49] (cm^{-1})	ω_{expt} [49] (cm^{-1})	ω_{th} [27] (cm^{-1})	ω_{expt} [57] (cm^{-1})	ω_{expt} [50] (cm^{-1})
S0	$B_g(126)$	$B_g(127)$	127	$A_g(126)$	127	124.2
S1	$A_g(143)$	$A_g(143)$	146	$B_g(143)$	147	143.8
S2	$B_g(160)$	$B_g(158)$	160	$B_g(170)$	158	156.6
S3	$A_g(189)$	$A_g(188)$	189	–	189	187.3
S4	$B_g(208)$	$B_g(204)$	209	$A_g(203)$	208	204.7
S5	$A_g(237)$	$A_g(230)$	235	$A_g(232)$	238	242.1
S6	$A_g(250)$	$A_g(252)$	252	–	251	260.4
S7	$B_g(307)$	$B_g(316)$	309	$B_g(315)$	309	306.2
S8	$A_g(328)$	$A_g(336)$	326	$A_g(334)$	329	326.3
S9	$A_g(347)$	$A_g(355)$	349	–	349	345.8
S10	$A_g(373)$	$A_g(380)$	373	$B_g(378)$	374	370.7
S11	$B_g(397)$	$B_g(389)$	397	$B_g(394)$	398	394.8
S12	$A_g(423)$	$A_g(423)$	426	–	–	420.7
S13	$B_g(439)$	$B_g(427)$	439	–	440	436.4
S14	$A_g(768)$	$A_g(784)$	768	–	770	766.5
S15	$B_g(791)$	$B_g(799)$	790	–	794	792.1
S16	$A_g(819)$	$A_g(806)$	819	–	819	817.5
S17	$A_g(841)$	$A_g(836)$	843	–	–	840.9
S18	$B_g(858)$	$B_g(861)$	855	$A_g(865)$	859	856.5
S19	$B_g(881)$	$B_g(892)$	882	$A_g(883)$	–	–

elements and their homogeneity in all the $LaV_{1-x}Nb_xO_4$ ($x = 0$–0.2) samples.

In Fig. 3(a) we present the room temperature Raman spectra of $LaV_{1-x}Nb_xO_4$ ($x = 0$–0.2) samples, which are shifted vertically for a clear presentation, and the left and right insets in this graph highlight the enhancement in the Raman spectral intensity with the Nb substitution and marked with the red arrows. The recorded spectra were deconvoluted and fitted using the Lorentzian peak shape function in Figs. 3(b)–3(f), with 20 individual Raman modes marked with S0–S19. It was found that 14 Raman peaks are between 100–600 cm^{-1} and 6 peaks are in the range of 750–900 cm^{-1}, which have been listed in Table II. In the $LaVO_4$ monazite structure, all the atoms possess 4*e* Wyckoff position and the symmetry decomposition of the zone center phonons are obtained using the point group symmetry of $2/m$ [49]. According to the group theory calculations, m-$LaVO_4$ consists of 72 vibrational modes ($18B_u + 18A_u + 18A_g + 18B_g$), which includes 3 acoustic modes ($A_u + 2B_u$), 33 infrared-active modes ($16B_u + 17A_u$), and 36 Raman active modes ($18A_g + 18B_g$) [55,56]. Here we are using the Mulliken symbols, where notations A and B represent that the vibrations are symmetric and antisymmetric with respect to the principal axis of symmetry, respectively. And the subscripts g and u represent that the vibrations are symmetric and antisymmetric with respect to a center of symmetry, respectively. One can differentiate A_g and B_g modes experimentally using the polarized Raman measurements. For the m-$LaVO_4$ compound there have been few reports on the Raman spectra [27,49,50,57], and we found a good agreement between our observed data and those in Refs. [49,57]. In RVO_4, the Raman modes can be classified as internal and external modes. The RVO_4 can be considered as composed of two sublattices, R and VO_4 units where the internal modes are due to vibration of VO_4 unit only, while external modes are due to the vibrations of both R and VO_4 units. In an ideal situation the modes due to the strong V-O bond in VO_4^{3-} tetrahedron were measured in a saturated aqueous solution of Na_3VO_4, which can be characterized as $\nu_1(A_1)$, $\nu_2(E)$, $\nu_3(F_2)$, and $\nu_4(F_2)$. The position and other details of these Raman modes can be found in Ref. [58]. The vibrational spectra of $LaVO_4$ can be divided into three groups, (i) the low-frequency (<240 cm^{-1}) region, (ii) the middle-frequency (270–450 cm^{-1}) region, and (iii) the high-frequency region (850–970 cm^{-1}), which are predominantly due to the translation of La atoms, the bending vibration of O-V-O bonds, and stretching vibration of O-V-O bonds, respectively [27]. The higher frequency stretching and bending modes are due to the shortest V-O bonds. In the m-$LaVO_4$, the Raman spectra are complex due to the presence of distorted VO_4 tetrahedron having four different V-O bond lengths. However, some modes are related to the tetrahedral symmetry like most intense A_g (ν_1) breathing mode at 858 cm^{-1}, A_g (ν_2) bending mode at 373 cm^{-1}, and the antisymmetric B_g (ν_4) mode at 439 cm^{-1}[49]. Also, Errandonea *et al.* found that no mode possesses pure ν_3 characteristics, there exists always a mixture of ν_1 and ν_3 modes [49]. We have compared the peak positions

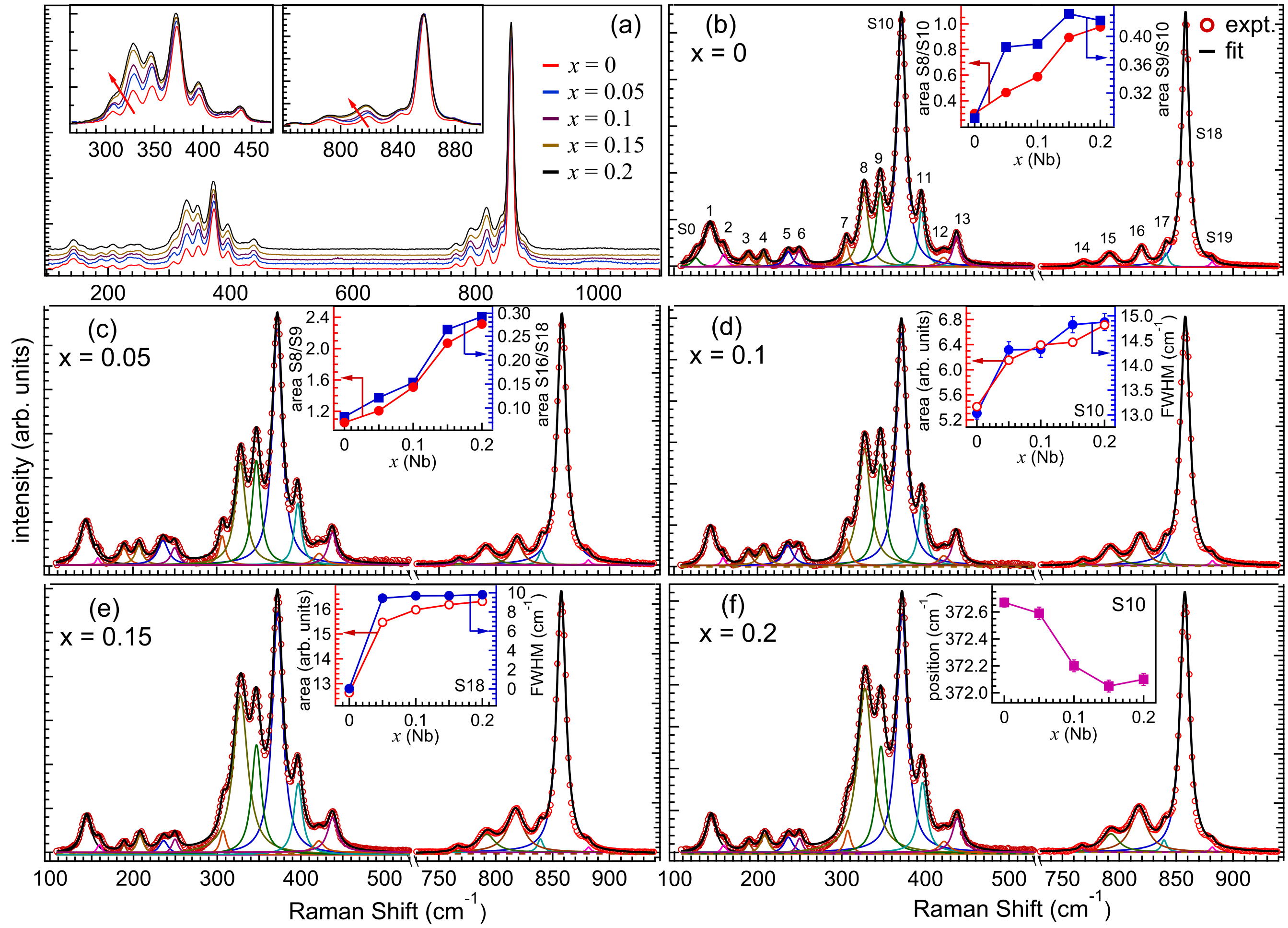

FIG. 3. (a) The room temperature Raman spectra of $LaV_{1-x}Nb_xO_4$ ($x = 0$–0.2) samples, left and right inset present a closer view of the as-recorded Raman modes in the lower (250–470 cm^{-1}) and higher (760–910 cm^{-1}) wave number regions, respectively. (b)–(f) Solid lines present the fitted individual modes of the recorded Raman spectra for $LaV_{1-x}Nb_xO_4$ ($x = 0$–0.2) samples, respectively, using the Lorentzian peak function and solid thick black line presents the total fit of the measured spectra. Insets in (b) present the variation of the relative area of S8/S10 and S9/S10 Raman modes with x on the left and right axis, respectively. (c) The dependence of relative area of S8/S9 and S16/S18 Raman modes with x on the left and right axis, respectively. (d) and (e) The variation of the integrated area and FWHM values for the S10 (373 cm^{-1}) and S18 (858 cm^{-1}) individual Raman modes with x plotted on the left and right axis, respectively. (f) The variation of the peak position of the S10 individual Raman mode with x, plots in the insets are marked with arrows to their respective axis.

of individual Raman modes from the reported experimental [49,50,57] and theoretical [27,49] values in Table II. Here our experimental values (ω_{obs}) are found to be in close agreement with Ref. [49]; therefore used for the mode assignment.

Furthermore, we have analyzed the variation in the integrated area of the selected Raman modes and their full-width-at-half-maximum (FWHM) with the Nb concentration ($x = 0$–0.2). We observe that the S0 (A_g) individual mode (126 cm^{-1}) is only present for the $x = 0$ sample and completely disappears for the Nb substituted samples ($x > 0$). This Raman mode is attributed to the translational of the La atoms, which indicates that the emergence of an additional phase with Nb substitution diminishes the intensity of this mode. Moreover, we found that the major peaks, which have the significant intensity contribution in the Raman spectra, i.e., S8, S9, S10, S15, S16, and S18 exhibit a monotonous enhancement in the integrated intensity as well as in the full-width-at-half-maximum (FWHM) with the increase of Nb concentration. This behavior is related to the fact that the increase in the scheelite-tetragonal phase with Nb substitution is responsible for the enhancement in the Raman modes of the Nb substituted samples. These monotonous effects on the vibrational spectra are correlated to the substitution induced deformation of the VO_4^{3-} tetrahedra and also can be seen in the FTIR spectra of the Nb substituted samples, discussed later. To see the variation in the intensity of S8 and S9 Raman modes with x, we plot their relative integrated area ratios as compared to the intense S10 mode on the left and right axis of the inset in Fig. 3(b). We found an enhancement in the relative area ratio of S8/S10 and S9/S10 modes with increasing x, see the inset in Fig. 3(b). It can be seen that the intensity of the S8 mode at 328 cm^{-1}, which is lower as compared to the S9 mode for the $x = 0$ sample, gradually increases with x and becomes higher for the $x = 0.2$ sample [see Figs. 3(b)–3(f)]. Therefore, we present the variation of the relative integrated area ratio of the Raman modes S8 and S9 on the left axis of the inset in Fig. 3(c), which was found to increase with the x. Similarly, the variation of the relative area ratio of S16 Raman mode with respect to the most-intense S18 mode is shown with x on the right axis of the inset in Fig. 3(c), which exhibits an increasing trend. These results indicate that the Nb substitution-induced emergence of the scheelite-tetragonal phase enhances the intensity of the selected Raman modes significantly with x. Furthermore, we analyze the behavior of the most intense Raman modes in the lower and higher wave number region, i.e., S10 (373 cm^{-1}) and S18 (858 cm^{-1}). A variation of the integrated area and FWHM values of S10 (A_g) mode with x is shown on the left and right axis, respectively [see inset of Fig. 3(d)]. We observe that the integrated area and FWHM values of A_g bending mode (S10) increase monotonically with the x. Also, we present the behavior of the peak position of S10 mode [see inset of Fig. 3(f)] with x and found a monotonous decrease in the peak position, which indicates that the A_g bending mode frequency decreases with deformation of VO$_4$ tetrahedra owing to the Nb substitution. Interestingly, for the S18 Raman mode (B_g) we found that the area and FWHM values exhibit a jump in the increment from the $x = 0$ to 0.05 sample, and then a monotonous increase in the values with the Nb concentration, see inset of Fig. 3(e). However, we found that the position of the S18 mode does not change despite the Nb substitution in the system (not shown), i.e., breathing vibrations associated with this mode are unaffected due to tetrahedral distortions. In addition to that, we have also investigated the peak position of the other fitted components with the Nb substitution, and found that there is no significant shift in the peak position of the S7, S8, S11, S12, S13, S15, and S20 Raman modes, whereas S9, S16, and S17 (all A_g) Raman modes exhibit a monotonous change with x (not shown here). The most intense S10 (A_g) and S18 (B_g) Raman modes manifest a remarkable change in the integrated area/FWHM with the Nb substitution in the VO$_4$ tetrahedra. These results further motivate us to investigate the local structure of these samples using x-ray absorption spectroscopy (XAS).

Therefore, the XAS measurements were performed for the La L_2, Nb K, and La L_3 + V K edges at room temperature for the $x = 0$ and 0.2 samples. We have calibrated each spectrum with the reference metal foils utilizing the maxima in the first-order derivative about the inflection near the edge jump. The normalized x-ray absorption spectra for LaVO$_4$ and reference La$_2$O$_3$ samples measured at the La L_2 edge (5891 eV) are presented in Fig. 4(a), where the inset shows the derivative about the first inflection near the edge jump and a solid line along the maxima (5907.9 eV) affirm that La cations exist in the trivalent oxidation state analogous to the La$_2$O$_3$ sample. As the photon energies of the V K edge (5465 eV) and La L_3 edge (5483 eV) are close to each other, an absorption measurement at one of them will eventually result in the strongly overlapped absorption spectra corresponding to both edges for the LaVO$_4$ sample. In Fig. 4(b) we present the normalized absorption spectra at these (V K and La L_3) edges for the LaVO$_4$ sample as well as for V$_2$O$_5$ as a reference. A pre-edge peak (near 5469.8 eV) in Fig. 4(b) appears due to the tetrahedral coordination of V ions in the monoclinic structure and confirms the d^0 configuration consistent with the earlier reports, as the intensity of the pre-edge feature is highest for the d^0 compounds and monotonously decreases to zero for d^{10} configuration [59,60]. This pre-edge peak in the V K edge emerges due to the electric dipolar transition to the p component in the p-d hybridized orbitals and some smaller contributions arise from the quadrupolar transitions within the same orbitals [60]. Note that this pre-edge feature is solely emerging due to the V K edge and unaffected by the contributions from the La L_3 edge. A comparison of the measured spectra with reference V$_2$O$_5$ sample at the pre-edge peak (near 5469 eV) in the left inset and the first-order derivative in the right inset of Fig. 4(b) portray a 5+ oxidation state of V ions similar to the reference V$_2$O$_5$ sample. Furthermore, we have recorded the absorption spectrum of the Nb K edge (18986 eV) for the LaV$_{0.8}$Nb$_{0.2}$O$_4$ sample having the highest Nb concentration and compared the maxima in the first-order derivative (around 18991 eV) with the reference Nb$_2$O$_5$ sample in Fig. 4(c), which reveals that the Nb ions in our sample exist in the 5+ oxidation state. Moreover, we have performed the curve fitting of the Nb K edge extended x-ray absorption fine structure (EXAFS) for the $x = 0.2$ sample using the Artemis program [61] up to the radial distance of 4.1 Å, as shown in Fig. 4(d). Note that the fitted spectrum is not corrected with backscattered and central phase shifts. In the curve-fitting procedure the atomic scattering paths were generated using the FEFF software with the help of results obtained from the Rietveld refinement of XRD pattern for the $x = 0.2$ sample, which shows both monoclinic (72%) and scheelite-tetragonal (28%) phases. Our analysis manifest that in the monoclinic phase there are four unequal V/Nb-O bond lengths available in a group of two sets, i.e., 3×1.804 and 1×1.749 Å, while for the scheelite-tetragonal

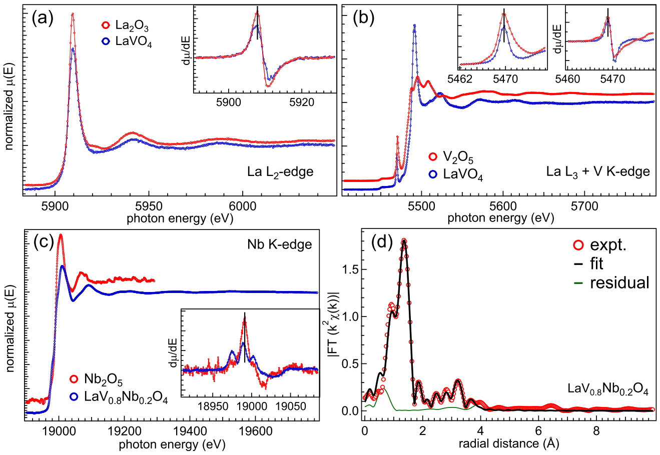

FIG. 4. The room temperature x-ray absorption spectra recorded in the transmission mode for (a) LaVO$_4$ and reference La$_2$O$_3$ samples at La L_2 edge, inset shows a comparison of the peak position in the first-order derivatives. (b) The combined La L_3 and V K edges of LaVO$_4$ and V$_2$O$_5$ samples where the left inset highlights the pre-edge peak and the right inset exhibit the comparison of maximum obtained in the first-order derivative. (c) The Nb K edge of LaV$_{0.8}$Nb$_{0.2}$O$_4$ and Nb$_2$O$_5$ samples where the inset shows a closer view of the maxima in the first-order derivative. (d) The Fourier transform of the EXAFS spectrum at the Nb K edge along with curve fitting for the LaV$_{0.8}$Nb$_{0.2}$O$_4$ sample. Note that the reference spectrum in the main panels (a)–(c) is vertically shifted by a constant factor of 0.1 for clear presentation.

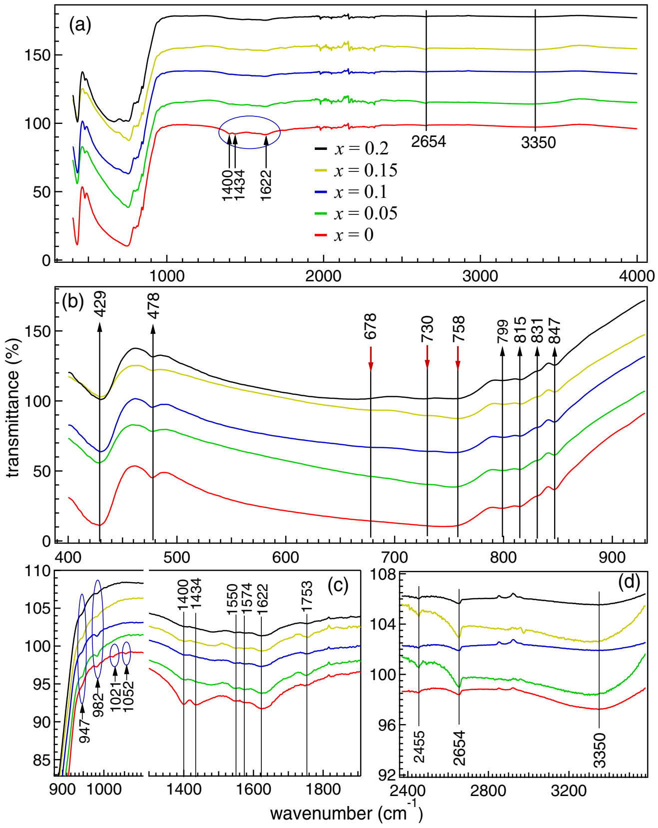

FIG. 5. (a) The Fourier transform infrared (FTIR) spectra of LaV$_{1-x}$Nb$_x$O$_4$ (x = 0–0.2) samples measured at room temperature. (b) Highlights the range between 390–930 cm^{-1}, where black arrows mark IR modes observed for all samples and new modes due to Nb substitution are marked with the red arrows. (c) and (d) The IR modes between 880–1908 cm^{-1} and 2370–3580 cm^{-1}, respectively. The spectra have been shifted vertically for clear presentation.

phase we obtained that the tetrahedra consist of four equal bonds with the values 4×1.842 and 4×2.491 Å. These values of bond lengths appear due to the cumulative contribution in the atomic absorption process from the oxygen atoms present in the vicinity of the absorbing Nb atoms.

Now, in order to validate the structure and composition, as well as to look for the possibility of infrared active modes, we perform the Fourier-transform infrared (FTIR) measurements of all the samples, as shown in Fig. 5. The as-recorded FTIR spectra in Fig. 5 are vertically shifted for clear presentation, while closer views are presented in Figs. 5(b)–5(d). All the well-resolved individual peaks are marked with the black vertical arrows, whereas the additional peaks emerging with Nb substitution are marked with the red arrows [see Fig. 5(b)]. The obtained spectra are similar to the other orthovanadate compounds, i.e., RVO$_4$ (R = Y, Ce-Yb) [32] and also with the compounds which possess the isolated tetrahedral VO$_4^{3-}$ groups, e.g., multimetal orthovanadates [62,63]. However, the FTIR spectra in compounds are modified due to variation in the site symmetry of VO$_4^{3-}$ anion as compared to the free ions and the parent sample. As discussed above, the monoclinic LaVO$_4$ crystallizes into $P2_1/n$ ($P121/n1$) space group, which manifests a primitive unit cell associated with the twofold screw axis along the unique axis b, and a glide plane n perpendicular to the b direction. The point group symmetry associated with the $P2_1/n$ space group is $2/m$ [49], which can be visualized as a mirror plane perpendicular to the twofold rotation axis. Therefore, the VO$_4^{3-}$ anion groups can be visualized at these point group symmetry positions in the monoclinic structure of LaVO$_4$ [see Fig. 1(f)]. In this regard, a detailed description of the point group symmetries for the different crystal systems of tetrahedral XO$_4^{3-}$ ions can be found in Ref. [64].

Moreover, the stretching (ν_1 and ν_3) and bending (ν_2 and ν_4) vibrations in the VO$_4^{3-}$ tetrahedra are associated with the O-V-O bonds, which exhibit the characteristic IR peaks for the different orthovanadate compounds in the range of 700–1100 cm^{-1} and 400–700 cm^{-1}, respectively. In the recorded spectra of all the samples, we observe the well-resolved strong and sharp bands at 429 and 478 cm^{-1}, which correspond to the ν_4 bending vibrations of VO$_4^{3-}$ tetrahedra [27,65]. Also, the wide bands between 700–1100 cm^{-1} are clearly observed, where a peak at 799 cm^{-1} quantifies the antisymmetric stretching along with the other overlapped peaks near 815, 831, and 847 cm^{-1} correspond to the ν_3 stretching vibrations of the VO$_4^{3-}$ tetrahedra [27,62,65], as marked by arrows in Fig. 5(b). In Fig. 5(c) we indicate four minima at positions 947, 982, 1021, and 1052 cm^{-1} in which modes 947 and 982 cm^{-1} appear due to the stretching vibrations of O-V-O bonds [27,30], and the other small modes near 1021 and 1052 cm^{-1} in the $x = 0$ sample appear due to the surface impurities from V$_2$O$_5$ [62] and C-O vibration [66], respectively. Furthermore, the modes at wave numbers 1400, 1434, 1550, 1574, 1622, 1753, 2455, 2654, and 3350 cm^{-1} are observed in FTIR spectra and marked by solid black lines in Figs. 5(c) and 5(d). Here the 1400 and 1434 cm^{-1} peaks appear due to the symmetric and antisymmetric vibrations of carboxylate groups, which emerge due to the reactive surface of LaVO$_4$ with CO$_2$ in air to form carbonate species, and the peaks at 1550 and 1574 cm^{-1} correspond to the asymmetrical bond stretching of carboxylate bidentate [67]. A strong band at 1622 cm^{-1} corresponds to the O-H bending vibrations from adsorbed water molecules [66,67]. A small peak at 1753 cm^{-1} is related to the C=O stretching vibrations [68], and the mode near 2455 cm^{-1} is generally associated with the vibrations from the hydrides [69]. The modes near 2654 cm^{-1} are related to the CH$_2$ stretching vibration and the broad minimum near 3350 cm^{-1} is attributed to the O-H stretching arising from the water absorption [66,67]. We can see that these bands (between 1400 and 3350 cm^{-1}) persist in all the samples, since our samples are sintered at such a high temperature, i.e., 1250 °C, therefore these modes are expected to be associated with the surface absorbed impurities of carbon and water. It is a little difficult to assign each spectral component to a specific type of vibrational mode and especially in the stretching range of vibrations. In the group theory calculations for the vibrational properties, the origin of the IR modes is associated with the crystal symmetry of the LaVO$_4$ compound. So, due to the lower symmetry of the m-LaVO$_4$ phase ($2/m$), a total of 33 IR active modes are predicted, where strongly overlapped IR active modes appear in the form of a wide band [27]. The addition of Nb cations will distort the VO$_4$ tetrahedra and that results in the observed changes in the IR spectra of substituted samples. In the present case, all the substituted samples are in

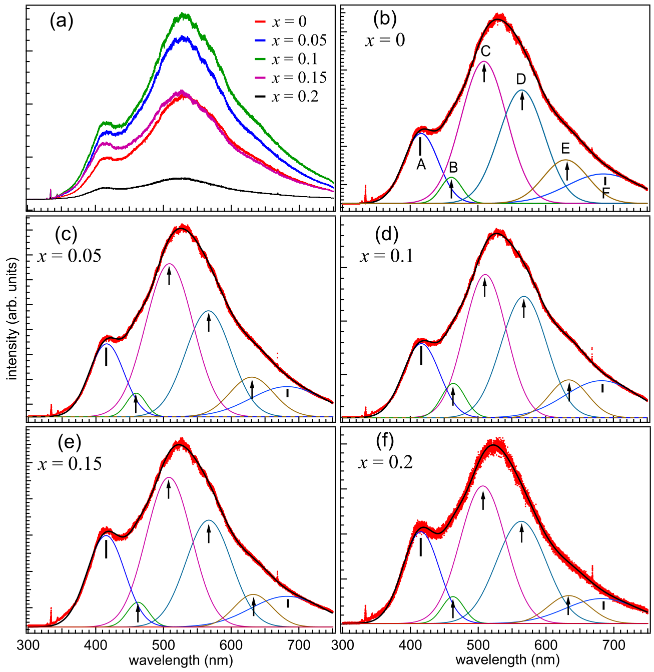

FIG. 6. (a) A comparison of the photoluminescence (PL) spectra of $LaV_{1-x}Nb_xO_4$ ($x = 0$–0.2) samples measured at room temperature using 325 nm excitation wavelength. (b)–(f) Deconvoluted and fitted PL spectra with six Gaussian peaks (A–F) for the $x = 0$–0.2 samples, respectively.

a mixed phase of monoclinic and scheelite-tetragonal in a certain proportion, as summarized in Table I. Here we found the emergence of three new peaks for the Nb substituted samples at 678, 730, and 758 cm^{-1}, which were absent for the $x = 0$ sample, these features are marked by red arrows in Fig. 5(b). These additional peaks in the IR spectra appear due to the additional symmetry modes of the scheelite-tetragonal phase in the Nb substituted samples and have their contribution from the $LaNbO_4$ phase [70]. The intensity of these peaks enhance monotonically with the Nb substitution. However, the IR mode at 478 cm^{-1} diminish in intensity with the Nb substitution. An overall change in the FTIR spectra including appearance of additional peaks [highlighted by red arrows in Fig. 5(b)], and variation in the intensity of modes at 478 and near 800 cm^{-1} are attributed to the effect of Nb substitution at the V site in $LaVO_4$ sample.

In order to understand the photoluminescence (PL) behavior, the room temperature PL spectra of $LaV_{1-x}Nb_xO_4$ ($x = 0$–0.2) samples were recorded in a spectral range of 300–750 nm using an excitation wavelength of $\lambda_{\mathrm{ex}} = 325$ nm [see Fig. 6(a)]. We observe a broad asymmetric and strongly overlapped peak centered near 540 nm with one small peak at a lower wavelength side near 415 nm (see Fig. 6). The strong emission in the PL spectra manifest the rapid recombination of electron-hole pairs [12]. The observed spectra are complex in nature having several strongly overlapped components, which emerge due to the transitions from a more complicated energy scheme. The observed spectrum for the $x = 0$ sample is analogous to the earlier reports, where several groups have observed the strongly overlapped bands centered near 540 nm [65,71,72]; however, a small kink near 415 nm is not observed in the literature. The broad peak shape is related to the several d-f transitions of the lanthanum orthovanadate compound [73]. We have deconvoluted and fitted the measured PL spectra using six Gaussian peaks, as marked by alphabets A–F and shown in Figs. 6(b)–6(f) for the $x = 0$–0.2 samples, respectively. The position of four peaks (B–E, marked by arrows) are taken from the related reference from the literature [25,71,72], while two peaks (A and F, marked by vertical lines) in the respective ends are inserted to fit the data with the minimum number of Gaussian peaks. The presence of six peaks in the deconvoluted PL spectra indicate the availability of more than one recombination centers for the electron-hole pairs, as the emission and excitation in these samples are all governed by the VO_4^{3-} tetrahedron having the T_d symmetry. Interestingly, the V^{5+} molecular orbitals consist of a ground state $^1A_1$ and four excited states named as $^1T_1$, $^1T_2$, $^3T_1$, and $^3T_2$ [74]. Among these states, the transitions related to the absorption process, i.e., $^1T_1$, $^1T_2 \leftarrow {}^1A_1$ are allowed, whereas the emission process transitions, i.e., $^3T_1$, $^3T_2 \rightarrow {}^1A_1$ are forbidden for the ideal T_d symmetry in terms of the spin-selection rule ($\Delta S = 0$). However, in the experimental observation we found that these forbidden transitions become partially allowed due to the distortion of VO_4^{3-} from the ideal state, which in turn changes the strength of spin-orbit coupling as it depends on the central-field potential of atoms as well as their spin and orbital angular momenta [74,75]. Interestingly, the tetrahedral distortion in VO_4^{3-} caused due to cationic substitution enhances the spin-orbit interaction and hence the intensity of the forbidden transitions is observed significantly higher in these compounds. These transitions are related to bands observed near the 570 and 635 nm [65]. Moreover, in m-$LaVO_4$ two bands at 550–650 nm and 650–700 nm are attributed to the $^5D_0 \rightarrow {}^7F_1$ and $^5D_0 \rightarrow {}^7F_2$ transitions, respectively [76]. The first is broadband which displays transitions of excited $5d$ states to the $^2F_{5/2}$ ground state, and last is small band related to $^5D_0 \rightarrow {}^7F_4$ transition [73,76]. The peak near 460 nm is related to the electron transitions between $^1T_1 \rightarrow {}^1A_1$ states [71]. We observe that for the $x = 0.1$ sample, the intensity of the emission spectra increases and FWHM decreases, indicating the reduction in the recombination centers. However, for the $x = 0.2$ sample, the PL intensity decreases and FWHM increases, which suggests the increase in the recombination centers for the electron-hole pairs. We found that the peak near 415 nm corresponds to the 2.98 eV of photon energy is related to the electron transition in V_2O_5 [77].

Finally, in order to find the band gap we perform the diffuse reflectance measurements of all the prepared $LaV_{1-x}Nb_xO_4$ ($x = 0$–0.2) samples sintered at 1250 °C. The recorded diffuse reflectance spectra were utilized to estimate the Kubelka-Munk (K-M) function [$F(R_\infty)$], which can be defined in terms of diffuse semi-infinite reflectance, i.e., $R_\infty = R_{\mathrm{sample}}/R_{\mathrm{standard}}$ as [78]

$$F(R_\infty) = (1 - R_\infty)^2/(2R_\infty).$$

Here we have used TiO_2 as a standard sample in our measurements. The band gap of samples can be estimated from the absorption threshold energy (given by the x-axis intercept) in

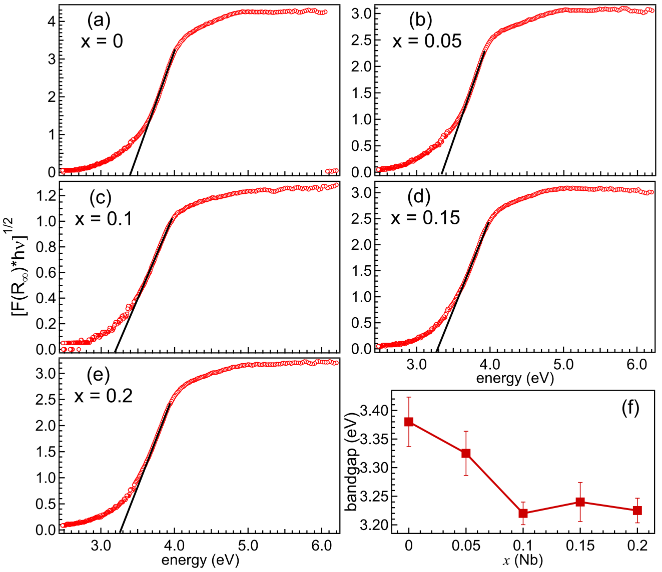

FIG. 7. (a)–(e) The Kubelka-Munk plots for the polycrystalline $LaV_{1-x}Nb_xO_4$ ($x = 0$–0.2) samples obtained from the diffused reflectance spectroscopy data, and (f) the optical band gap as a function of x calculated from the x-axis intercept along the optical absorption edge in the Tauc plot.

the Tauc plot, which can be written as

$$(\alpha h\nu) = k(h\nu - E_g)^\eta,$$

where α, ν, k, E_g, and η are the absorption coefficient, frequency, absorption constant, band gap energy, and exponent of the equation [79]. The value of this exponent η depends upon the type of the transition/band gap in the material and can have values of 1/2, 2, 3/2, and 3 for the direct allowed, indirect allowed, direct forbidden, and indirect forbidden transitions, respectively [79]. In the case of diffuse reflectance spectra the α in Tauc plot can be replaced by the K-M function to estimate the band gap of the material [80]. Since our material has an indirect band gap so the value of η is 2, therefore we have plotted the $[F(R_\infty) \times h\nu]^{1/2}$ versus E for each sample in Figs. 7(a)–7(e). The x-axis intercept of the linear fitting [presented as a solid black line in each graph of Figs. 7(a)–7(e)] along the optical absorption edge for samples $LaV_{1-x}Nb_xO_4$ ($x = 0$–0.2) gives an estimation of optical band gap. We present the variation of the optical band gap of these samples with the Nb concentration (x) in Fig. 7(f). The band gap value of the parent m-$LaVO_4$ ($x = 0$) compound is about 3.4 eV, which is consistent with the reported experimental value of 3.5 ± 0.2 eV in Ref. [81]. Moreover, the band gap value decreases up to the $x = 0.1$ sample to 3.22 eV and then almost constant for the samples with $x > 0.1$ (3.24 eV). The optical absorption property of a semiconductor, which is relevant to the electronic structure serves as a key factor in determination of the photocatalytic activity [12,13,80].

IV. CONCLUSIONS

In conclusion we have successfully prepared polycrystalline $LaV_{1-x}Nb_xO_4$ ($x = 0$–0.2) samples by solid-state reaction method including the pure scheelite-tetragonal phase. The room temperature x-ray absorption measurements reveal that the La cation exists in a trivalent oxidation state, while V and Nb cations have their 5+ oxidation state in a tetrahedral coordination. The substitution of Nb ions in place of V ions reveals a structural phase transformation due to its larger size as compared to the V^{5+}. The Rietveld refinement of room temperature x-ray diffraction patterns demonstrate that the $x = 0$ sample exist in a monoclinic (m) phase, whereas for the $x = 0.05$–0.2, both monoclinic and scheelite-tetragonal (s-t) phases coexist in a certain fraction. Interestingly, a monotonous enhancement in the Raman spectral intensity with Nb substitution is correlated with the substitution induced increase in the s-t phase. The room temperature photoluminescence measurements on these samples exhibit a broad spectra, the deconvolution of these spectra using six Gaussian peaks designate the availability of more than one electron-hole pairs recombination center. Moreover, the FTIR spectra indicate that the Nb substitution gives origin to some additional infrared active modes owing to the deformation of the VO_4^{3-} tetrahedra.

ACKNOWLEDGMENTS

H.D. and R.S. are grateful to MHRD and DST-INSPIRE, respectively for their financial support through fellowship. Authors thank FIST (DST, Govt. of India) UFO scheme of IIT Delhi for providing Raman facility at physics department. We acknowledge the Central Research Facility (CRF) for EDX, Physics Department for XRD, and Nanoscale Research Facility (NRF) for PL, FTIR, and UV-Vis facilities. We thank Ravi Kumar and S. N. Jha for help and support during XAS measurements at RRCAT, India. R.S.D. acknowledges the financial support from SERB-DST through Early Career Research (ECR) Award (Project No. ECR/2015/000159) and UGC-DAE CSR Indore through CRS Project No. CSR-IC-ISUM-36/CRS-319/2019-20/1371. A high temperature furnace (from Nabertherm GmbH, Germany) was used for sample preparation, supported from BRNS through DAE Young Scientist Research Award (Project Sanction No. 34/20/12/2015/BRNS).

---

[1] Y. Zhao, M. Shao, S. Liu, Z. Zhang, and H. Lin, Hydrothermal synthesis of lanthanide orthovanadate: $EuVO_4$ particles and their fluorescence application, Cryst. Eng. Commun. **14**, 8033 (2012).

[2] G. Wang, Q. Peng, and Y. Li, Lanthanide-doped nanocrystals: Synthesis, optical-magnetic properties, and applications, Acc. Chem. Res. **44**, 322 (2011).

[3] B. Bulbul and S. Beyaz, Strong paramagnetic crystalline $LnVO_4$ (Ln: Gd, Tb, Dy, Ho, Er) nanoparticles synthesized by a fabricating method, Mater. Chem. Phys. **173**, 200 (2016).

[4] M. Yi, S.-K. Park, C.-Y. Seong, Y. Piao, and T. Yu, The general synthesis and characterization of rare earth orthovanadate nanocrystals and their electrochemical applications, J. Alloys Compd. **693**, 825 (2017).

[5] Y. Zhang, G. Li, X. Yang, H. Yang, Z. Lu, and R. Chen, Monoclinic $BiVO_4$ micro-/nanostructures: Microwave and ultrasonic wave combined synthesis and their visible-light photocatalytic activities, J. Alloys Compd. **551**, 544 (2013).

[6] D. Errandonea, R. Lacomba-Perales, J. Ruiz-Fuertes, A. Segura, S. N. Achary, and A. K. Tyagi, High-pressure structural investigation of several zircon-type orthovanadates, Phys. Rev. B **79**, 184104 (2009).

[7] D. Errandonea and A. B. Garg, Recent progress on the characterization of the high-pressure behaviour of AVO_4 orthovanadates, Prog. Mater. Sci. **97**, 123 (2018).

[8] M. B. Smirnov, A. P. Mirgorodsky, V. Yu. Kazimirov, and R. Guinebretiére, Bond-switching mechanism for the zircon-scheelite phase transition, Phys. Rev. B **78**, 094109 (2008).

[9] C. W. Kim, D. K. Kim, W. J. Shin, M. J. Choi, Y. S. Kang, and Y. S. Kang, Phosphor positioning for effective wavelength conversion in dye-sensitized solar cells, Nano Energy **13**, 573 (2015).

[10] M. Zahedifar, Z. Chamanzadeh, and S. M. H. Mashkani, Synthesis of $LaVO_4$:Dy^{3+} luminescent nanostructure and optimization of its performance as down-converter in dye-sensitized solar cells, J. Lumin. **135**, 66 (2013).

[11] M. Yu, J. Lin, and S. B. Wang, Effects of x and R^{3+} on the luminescent properties of Eu^{3+} in nanocrystalline $YV_xP_{1-x}O_4$:Eu^{3+} and RVO_4:Eu^{3+} thin-film phosphors, Appl. Phys. A **80**, 353 (2005).

[12] Y. He, Y. Wang, L. Zhao, X. Wu, and Y. Wu, Preparation, characterization and activity evaluation of V_2O_5-$LaVO_4$ composites under visible light irradiation, J. Mol. Catal. A: Chem. **337**, 61 (2011).

[13] S. Mahapatra, G. Madras, and T. N. G. Row, Synthesis, characterization and photocatalytic activity of lanthanide (Ce, Pr and Nd) orthovanadates, Ind. Eng. Chem. Res. **46**, 1013 (2007).

[14] M. R. Dolgos, A. M. Paraskos, M. W. Stoltzfus, S. C. Yarnell, and P. M. Woodward, The electronic structures of vanadate salts: Cation substitution as a tool for band gap manipulation, J. Solid State Chem. **182**, 1964 (2009).

[15] H.-Y. Lin, Y.-F. Chen, and Y.-W. Chen, Water splitting reaction on NiO/$InVO_4$ under visible light irradiation, Int. J. Hydrogen Energy **32**, 86 (2007).

[16] C.-J. Jia, L.-D. Sun, L.-P. You, X.-C. Jiang, F. Luo, Y.-C. Pang, and C.-H. Yan, Selective synthesis of monazite- and zircon-type $LaVO_4$ nanocrystals, J. Phys. Chem. B **109**, 3284 (2005).

[17] W. Fan, X. Song, Y. Bu, S. Sun, and X. Zhao, Selected-control hydrothermal synthesis and formation mechanism of monazite- and zircon-type $LaVO_4$ nanocrystals, J. Phys. Chem. B **110**, 23247 (2006).

[18] R. K. Selvan, A. Gedanken, P. Anilkumar, G. Manikandan, and C. Karunakaran, Synthesis and characterization of rare earth orthovanadate (RVO_4; R = La, Ce, Nd, Sm, Eu & Gd) nanorods/nanocrystals/nanospindles by a facile sonochemical method and their catalytic properties, J. Cluster Sci. **20**, 291 (2009).

[19] C. E. Rice and W. R. Robinson, Lanthanum orthovanadate, Acta Cryst. B **32**, 2232 (1976).

[20] B. C. Chakoumakos, M. M. Abraham, and L. A. Boatner, Crystal structure refinements of zircon-type MVO_4 (M = Sc, Y, Ce, Pr, Nd, Tb, Ho, Er, Tm, Yb, Lu), J. Solid State Chem. **109**, 197 (1994).

[21] R. D. Shannon and C. T. Prewitt, Effective ionic radii in oxides and fluorides, Acta Cryst. B **25**, 925 (1969).

[22] R. C. Ropp and B. Carroll, Dimorphic lanthanum orthovanadate, J. Inorg. Nucl. Chem. **35**, 1153 (1973).

[23] W. Fan, X. Song, S. Sun, and X. Zhao, Microemulsion-mediated hydrothermal synthesis and characterization of zircon-type $LaVO_4$ nanowires, J. Solid State Chem. **180**, 284 (2007).

[24] A. H. Krumpel, E. van der Kolk, P. Dorenbos, P. Boutinaud, E. Cavalli, and M. Bettinelli, Energy level diagram for lanthanide-doped lanthanum orthovanadate, Mater. Sci. Eng. B **146**, 114 (2008).

[25] A. H. Krumpel, E. van der Kolk, E. Cavalli, P. Boutinaud, M. Bettinelli, and P. Dorenbos, Lanthanide $4f$-level location in AVO_4: Ln^{3+} (A = La, Gd, Lu) crystals, J. Phys.: Condens. Matter **21**, 115503 (2009).

[26] S. W. Park, H. K. Yang, J. W. Chung, Y. Chen, B. K. Moon, B. C. Choi, J. H. Jeong, and J. H. Kim, Photoluminescent properties of $LaVO_4$:Eu^{3+} by structural transformation, Physica B **405**, 4040 (2010).

[27] L. Sun, X. Zhao, Y. Li, P. Li, H. Sun, X. Cheng, and W. Fan, First-principles studies of electronic, optical, and vibrational properties of $LaVO_4$ polymorph, J. Appl. Phys. **108**, 093519 (2010).

[28] C. J. Jia, L. D. Sun, F. Luo, X. C. Jiang, L. H. Wei, and C. H. Yan, Structural transformation induced improved luminescent properties for $LaVO_4$: Eu nanocrystals, Appl. Phys. Lett. **84**, 5305 (2004).

[29] U. Rambabu, D. P. Amalnerkar, B. B. Kale, and S. Buddhudu, Fluorescence spectra of Eu^{3+}-doped $LnVO_4$ (Ln = La and Y) powder phosphors, Mater. Res. Bull. **35**, 929 (2000).

[30] G. Liu, X. Duan, H. Li, and H. Dong, Hydrothermal synthesis, characterization and optical properties of novel fishbone-like $LaVO_4$:Eu^{3+} nanocrystals, Mater. Chem. Phys. **115**, 165 (2009).

[31] X. Yin, H. Wang, T. Jiang, M. Xing, Y. Fu, Y. Tian, and X. Luo, Up-conversion luminescence properties and thermal effects of $LaVO_4$:Er^{3+} under 1550 nm excitation, Mater. Res. Bull. **86**, 228 (2017).

[32] J. Liu and Y. Li, Synthesis and self-assembly of luminescent Ln^{3+}-doped $LaVO_4$ uniform nanocrystals, Adv. Mater. **19**, 1118 (2007).

[33] A. Tymiński and T. Grzyb, Enhancement of the up-conversion luminescence in $LaVO_4$ nanomaterials by doping with M^{2+}, M^{4+} ($M^{2+} = Sr^{2+}, Ba^{2+}, Mg^{2+}$; $M^{4+} = Sn^{4+}$) ions, J. Alloys Compd. **782**, 69 (2019).

[34] R. Okram, N. Yaiphaba, R. S. Ningthoujam, and N. R. Singh, Is higher ratio of monoclinic to tetragonal in $LaVO_4$ a better luminescence host? Redispersion and polymer film formation, Inorg. Chem. **53**, 7204 (2014).

[35] S. Verma, B. N. Wani, and N. M. Gupta, Synthesis, characterisation, TPR/TPO and activity studies on $LaMn_xV_{1-x}O_{4-\delta}$– catalysts, Appl. Catal. A: Gen. **205**, 295 (2001).

[36] S. Ding, H. Zhang, Y. Chen, Q. Zhang, R. Dou, W. Liu, G. Sun, and D. Sun, Structure, electronic and optical properties of $LaNbO_4$: An experimental and first-principles study, Solid State Commun. **277**, 7 (2018).

[37] B. Yan and X. Z. Xiao, Matrix induced synthesis of $LaNbO_4$:Tb^{3+} phosphors by in situ composing hybrid precursors, Opt. Mater. **28**, 498 (2006).

[38] Y. J. Hsiao, T. H. Fang, Y. S. Chang, Y. H. Chang, C. H. Liu, L. W. Ji, and W. Y. Jywe, Structure and luminescent properties of $LaNbO_4$ synthesized by sol-gel process, J. Lumin. **126**, 866 (2007).

[39] G. Blasse and L. H. Brixner, Ultraviolet emission from ABO_4-type niobates, tantalates and tungstates, Chem. Phys. Lett. **173**, 409 (1990).

[40] L. Jian and C. M. Wayman, Monoclinic-to-tetragonal Phase transformation in a ceramic rare-earth orthoniobate, $LaNbO_4$, J. Am. Ceram. Soc. **80**, 803 (1997).

[41] M. Huse, A. W. B. Skilbred, M. Karlsson, S. G. Eriksson, T. Norby, R. Haugsrud, and C. S. Knee, Neutron diffraction study of the monoclinic to tetragonal structural transition in $LaNbO_4$ and its relation to proton mobility, J. Solid State Chem. **187**, 27 (2012).

[42] D. Errandonea, A. B. Garg, J. Pellicer-Porres, D. Martinez-Garcia, and C. Popescu, Monoclinic-tetragonal-monoclinic phase transitions in $Eu_{0.1}Bi_{0.9}VO_4$ under pressure, J. Phys.: Condens. Matter **31**, 485401 (2019).

[43] V. Panchal, D. Errandonea, A. Segura, P. Rodríguez-Hernandez, A. Muñoz, S. Lopez-Moreno, and M. Bettinelli, The electronic structure of zircon-type orthovanadates: Effects of high-pressure and cation substitution, J. Appl. Phys. **110**, 043723 (2011).

[44] J. R.-Carvajal, Recent advances in magnetic structure determination by neutron powder diffraction, Physica B **192**, 55 (1993).

[45] See Supplemental Material at http://link.aps.org/supplemental/10.1103/PhysRevB.103.174107 for further information about the comparison of XRD patterns of $LaV_{1-x}Nb_xO_4$ as a function of x and the Rietveld refinement for the $x = 0.2$ sample with $P2_1/n$ space group where the significant peaks in the difference pattern and corresponding Bragg positions validate the need of an additional phase with $I4_1/a$ space group.

[46] W. I. F. David, The high-temperature paraelastic structure of $LaNbO_4$, Mater. Res. Bull. **18**, 749 (1983).

[47] D. Guo, D. Zhou, W.-B. Li, L.-X. Pang, Y.-Z. Dai, and Z.-M. Qi, Phase evolution, crystal structure, and microwave dielectric properties of water-insoluble $(1-x)LaNbO_4$–$xLaVO_4$ $(0 \leqslant x \leqslant 0.9)$ ceramics, Inorg. Chem. **56**, 9321 (2017).

[48] A. B. Garg, R. Rao, T. Sakuntala, B. N. Wani, and V. Vijayakumar, Phase stability of $YbVO_4$ under pressure: *In situ* x-ray and Raman spectroscopic investigations, J. Appl. Phys. **106**, 063513 (2009).

[49] D. Errandonea, J. Pellicer-Porres, D. Martínez-García, J. Ruiz-Fuertes, A. Friedrich, W. Morgenroth, C. Popescu, P. Rodríguez-Hernández, A. Muñoz, and M. Bettinelli, Phase stability of lanthanum orthovanadate at high-pressure, J. Phys. Chem. C **120**, 13749 (2016).

[50] X. Cheng, D. Guo, S. Feng, K. Yang, Y. Wang, Y. Ren, and Y. Song, Structure and stability of monazite- and zircon-type $LaVO_4$ under hydrostatic pressure, Opt. Mater. **49**, 32 (2015).

[51] F. J. Manjón, D. Errandonea, N. Garro, J. Pellicer-Porres, P. Rodríguez-Hernández, S. Radescu, J. López-Solano, A. Mujica, and A. Muñoz, Lattice dynamics study of scheelite tungstates under high pressure. I. $BaWO_4$, Phys. Rev. B **74**, 144111 (2006).

[52] Z. Huang, L. Zhang, and W. Pan, Synthesis, lattice dynamics, and mechanical properties of a high-pressure scheelite phase of RVO_4, Inorg. Chem. **51**, 11235 (2012).

[53] U. Müller, *Symmetry Relationships Between Crystal Structures: Applications of Crystallographic Group Theory in Crystal Chemistry* (Oxford University Press, Oxford, 2013).

[54] K. Momma and F. Izumi, VESTA 3 for three-dimensional visualization of crystal, volumetric and morphology, J. Appl. Crystallogr. **44**, 1272 (2011).

[55] C. C. Santos, E. N. Silva, A. P. Ayala, I. Guedes, P. S. Pizani, C.-K. Loong, and L. A. Boatner, Raman investigations of rare earth orthovanadates, J. Appl. Phys. **101**, 053511 (2007).

[56] V. Panchal, S. López-Moreno, D. Santamaría-Pérez, D. Errandonea, F. J. Manjón, P. Rodríguez-Hernandez, A. Muñoz, S. N. Achary, and A. K. Tyagi, Zircon to monazite phase transition in $CeVO_4$: X-ray diffraction and Raman-scattering measurements, Phys. Rev. B **84**, 024111 (2011).

[57] C. J. Jia, L. D. Sun, Z. G. Yan, Y. C. Pang, S. Z. Lü, and C. H. Yan, Monazite and zircon type $LaVO_4$:Eu nanocrystals-synthesis, luminescent properties, and spectroscopic identification of the Eu^{3+} sites, Eur. J. Inorg. Chem. **18**, 2626 (2010).

[58] S. J. A. Pope and Y. D. West, Comparison of the FT Raman spectra of inorganic tetrahedral ions over the temperature range 77 to 473 K, Spectrochim. Acta A **51**, 2027 (1995).

[59] M. Chandra, T. S. Khan, R. Shukla, S. Ahamad, A. Gupta, S. Basu, M. Ali Haider, and R. S. Dhaka, Diffusion coefficient and electrochemical performance of $NaVO_3$ anode in Li/Na batteries, Electrochem. Acta **331**, 135293 (2020).

[60] T. Yamamato, Assignment of pre-edge peaks in K-edge x-ray absorption spectra of 3d transition metal compounds: Electric dipole or quadrupole? X-Ray Spectrom. **37**, 572 (2008).

[61] B. Ravel and M. Newville, ATHENA, ARTEMIS, HEPHAESTUS: data analysis for x-ray absorption spectroscopy using IFEFFIT, J. Synchrotron Radiat. **12**, 537 (2005).

[62] Z. M. Fang, Q. Hong, Z. H. Zhou, S. J. Dai, W. Z. Weng, and H. L. Wan, Oxidative dehydrogenation of propane over a series of low-temperature rare earth orthovanadate catalysts prepared by the nitrate method, Catal. Lett. **61**, 39 (1999).

[63] L. Rghioui, L. Benarafa, J. El Jastimi, A. El Hajji, A. Lorriaux, and F. Wallart, Vibrational spectra and force field studies of $K_{1.125}Rb_{1.875}La(VO_4)_2$ vanadate, J. Mater. Environ. Sci. **3**, 58 (2012).

[64] A. Hezel and S. D. Ross, Forbidden transitions in the infra-red spectra of tetrahedral anions-III. Spectra-structure correlations in perchlorates, sulphates, and phosphates of the formula MXO_4, Spectrochim. Acta **22**, 1949 (1966).

[65] O. V. Chukova, S. G. Nedilko, A. A. Slepets, S. A. Nedilko, and T. A. Voitenko, Synthesis and properties of the $La_{1-x-y}Eu_yCa_xVO_4$ $(0 \leqslant x,\ y \leqslant 0.2)$ compounds, Nanoscale Res. Lett. **12**, 340 (2017).

[66] R. Okram, G. Phaomei, and N. Rajmuhon Singh, Water driven enhanced photoluminescence of Ln(=Dy^{3+}, Sm^{3+}) doped $LaVO_4$ nanoparticles and effect of Ba^{2+} co-doping, Mater. Sci. Eng. B **178**, 409 (2013).

[67] M. T.-González, A. Peacock, A. Miskowiec, D. A. Cullen, R. Copping, S. Mirzadeh, and S. M. Davern, Tailoring the radionuclide encapsulation and surface chemistry of $La(^{223}Ra)VO_4$ nanoparticles for targeted alpha therapy, J. Nanotheranostics **2**, 33 (2021).

[68] K. I. Hadjiivanov, D. A. Panayotov, M. Y. Mihaylov, E. Z. Ivanova, K. K. Chakarova, S. M. Andonova, and N. L. Drenchev, Power of infrared and Raman spectroscopies to

characterize metal-organic frameworks and investigate their interaction with guest molecules, Chem. Rev. **121**, 1286 (2021).

[69] J. Coates, Interpretation of infrared spectra, a practical approach, in *Encyclopedia of Analytical Chemistry: Applications, Theory and Instrumentation*, edited by R. A. Meyers (John Wiley & Sons, New York, 2006), Vol. 1, p. 10815.

[70] S. Tsunekawa, H. Takei, and M. Ishigame, Study of the room temperature phase of $LaNbO_4$ crystals, Mater. Res. Bull. **12**, 1098 (1977).

[71] O. Chukova, S. G. Nedilko, S. A. Nedilko, T. Voitenko, O. Gomenyuk, and V. Sheludko, Study of temperature behavior of luminescence emission of $LaVO_4$ and $La_{1-x}Eu_xVO_4$ powders, Solid State Phenom. **230**, 153 (2015).

[72] G. C. Gül and F. Kurtulus, $LaVO_4$, $LaPO_4$ and $LaBO_3$: Synthesis, Rietveld refinement, and comparison of optical properties, Optoelectron. Adv. Mat. **13**, 126 (2019).

[73] J. Zheng, Q. Cheng, S. Wu, Y. Zhuang, Z. Guo, Y. Lu, and C. Chen, Structure, electronic properties, luminescence and chromaticity investigations of rare earth doped $KMgBO_3$ phosphors, Mater. Chem. Phys. **165**, 168 (2015).

[74] T. Nakajima, M. Isobe, T. Tsuchiya, Y. Ueda, and T. Manabe, Correlation between luminescence quantum efficiency and structural properties of vanadate phosphors with chained, dimerized, and isolated VO_4 tetrahedra, J. Phys. Chem. C **114**, 5160 (2010).

[75] O. S. Ojambati, W. M. Deacon, R. Chikkaraddy, C. Readman, Q. Lin, Z. K.-Benda, E. Rosta, O. A. Scherman, and J. J. Baumberg, Breaking the selection rules of spin-forbidden molecular absorption in plasmonic nanocavities, ACS Photon. **7**, 2337 (2020).

[76] Y. He, J. Zhang, W. Zhou, J. Han, Z. Qiu, L. Yu, C. Rong, and S. Lian, Multicolor emission in a single-phase phosphor $Ca_3Al_2O_6$: Ce^{3+}, Li^+: Luminescence and site occupancy, J. Am. Ceram. Soc. **97**, 1517 (2014).

[77] T. K. Le, M. Kang, S. W. Han, and S. W. Kim, Highly intense room-temperature photoluminescence in V_2O_5 nanospheres, RSC Adv. **8**, 41317 (2018).

[78] V. P. Kubelka and F. Munk, Ein Beltrag zur Optik der Farbanstriche, Z. Tech. Physik **12**, 593 (1931).

[79] J. Tauc, R. Grigorovici, and A. Vancu, Optical properties and electronic structure of amorphous germanium, Phys. Status Solidi B **15**, 627 (1966).

[80] P. Makula, M. Pacia, and W. Macyk, How to correctly determine the band gap energy of modified semiconductor photocatalysts based on UV-Vis spectra, J. Phys. Chem. Lett. **9**, 6814 (2018).

[81] P. Parhi and V. Manivannan, Novel microwave initiated solid-state metathesis synthesis and characterization of lanthanide phosphates and vanadates, LMO_4 ($L = Y$, La and $M = V$, P), Solid State Sci. **10**, 1012 (2008).